



**HAL**  
open science

## Range-resolved detection of boundary layer stable water vapor isotopologues using a ground-based 1.98 $\mu\text{m}$ differential absorption LIDAR

Jonas Hamperl, Jean-Baptiste Dherbecourt, Myriam Raybaut, Julien Totems, Patrick Chazette, Laurence Régalia, Bruno Grouiez, Nicolas Geyskens, Oualid Aouji, Nadir Amarouche, et al.

### ► To cite this version:

Jonas Hamperl, Jean-Baptiste Dherbecourt, Myriam Raybaut, Julien Totems, Patrick Chazette, et al.. Range-resolved detection of boundary layer stable water vapor isotopologues using a ground-based 1.98  $\mu\text{m}$  differential absorption LIDAR. *Optics Express*, 2022, 30 (26), pp.47199-47215. 10.1364/oe.472451 . insu-03908665

**HAL Id: insu-03908665**

**<https://insu.hal.science/insu-03908665v1>**

Submitted on 20 Dec 2022

**HAL** is a multi-disciplinary open access archive for the deposit and dissemination of scientific research documents, whether they are published or not. The documents may come from teaching and research institutions in France or abroad, or from public or private research centers.

L'archive ouverte pluridisciplinaire **HAL**, est destinée au dépôt et à la diffusion de documents scientifiques de niveau recherche, publiés ou non, émanant des établissements d'enseignement et de recherche français ou étrangers, des laboratoires publics ou privés.



Distributed under a Creative Commons Attribution - NonCommercial 4.0 International License



# Range-resolved detection of boundary layer stable water vapor isotopologues using a ground-based 1.98 $\mu\text{m}$ differential absorption LIDAR

JONAS HAMPERL,<sup>1</sup> JEAN-BAPTISTE DHERBECOURT,<sup>1</sup>  
MYRIAM RAYBAUT,<sup>1</sup> JULIEN TOTEMS,<sup>2</sup> PATRICK CHAZETTE,<sup>2</sup>  
LAURENCE RÉGALIA,<sup>3</sup> BRUNO GROUIEZ,<sup>3</sup> NICOLAS GEYSKENS,<sup>4</sup>  
OUALID AOUJI,<sup>4</sup> NADIR AMAROUCHE,<sup>4</sup>  
JEAN-MICHEL MELKONIAN,<sup>1</sup>  ROSA SANTAGATA,<sup>1</sup>   
ANTOINE GODARD,<sup>5</sup>  CORINNE EVESQUE,<sup>6</sup>  
VALDAS PASISKEVICIUS,<sup>7</sup> AND CYRILLE FLAMANT<sup>8,\*</sup> 

<sup>1</sup>DPHY, ONERA, Université Paris-Saclay, Palaiseau, France

<sup>2</sup>Laboratoire des Sciences du Climat et de l'Environnement (LSCE), UMR 1572, CEA-CNRS-UVSQ, Gif-sur-Yvette, France

<sup>3</sup>Groupe de Spectrométrie Moléculaire et Atmosphérique (GSMA), UMR 7331, URCA, Reims, France

<sup>4</sup>Division Technique INSU (DT INSU), UPS 855, Meudon, France

<sup>5</sup>DSG, ONERA, Université Paris-Saclay, Palaiseau, France

<sup>6</sup>Institut Pierre-Simon Laplace (IPSL), FR636, Guyancourt, France

<sup>7</sup>KTH, Royal Institute of Technology, Roslagstullsbacken 21, 10691 Stockholm, Sweden

<sup>8</sup>Laboratoire Atmosphères, Milieux, Observations Spatiales (LATMOS), UMR 8190, CNRS-SU-UVSQ, Paris, France

\*[cyrille.flamant@latmos.ipsl.fr](mailto:cyrille.flamant@latmos.ipsl.fr)

**Abstract:** This paper presents a first demonstration of range-resolved differential absorption LIDAR (DIAL) measurements of the water vapor main isotopologue  $\text{H}_2^{16}\text{O}$  and the less abundant semi-heavy water isotopologue  $\text{HD}^{16}\text{O}$  with the aim of determining the isotopic ratio. The presented Water Vapor and Isotope Lidar (WaVIL) instrument is based on a parametric laser source emitting nanosecond pulses at 1.98  $\mu\text{m}$  and a direct-detection receiver utilizing a commercial InGaAs PIN photodiode. Vertical profiles of  $\text{H}_2^{16}\text{O}$  and  $\text{HD}^{16}\text{O}$  were acquired in the planetary boundary layer in the suburban Paris region up to a range of 1.5 km. For time averaging over 25 min, the achieved precision in the retrieved water vapor mixing ratio is  $0.1 \text{ g kg}^{-1}$  (2.5% relative error) at 0.4 km above ground level (a.g.l.) and  $0.6 \text{ g kg}^{-1}$  (20%) at 1 km a.g.l. for 150 m range bins along the LIDAR line of sight. For  $\text{HD}^{16}\text{O}$ , weaker absorption has to be balanced with coarser vertical resolution (600 m range bins) in order to achieve similar relative precision. From the DIAL measurements of  $\text{H}_2^{16}\text{O}$  and  $\text{HD}^{16}\text{O}$ , the isotopic abundance  $\delta\text{D}$  was estimated as  $-51\text{‰}$  at 0.4 km above the ground and  $-119\text{‰}$  in the upper part of the boundary layer at 1.3 km a.g.l. Random and systematic errors are discussed in the form of an error budget, which shows that further instrumental improvements are required on the challenging path towards DIAL-profiling of the isotopic abundance with range resolution and precision suitable for water cycle studies.

© 2022 Optica Publishing Group under the terms of the [Optica Open Access Publishing Agreement](#)

## 1. Introduction

Water vapor in the atmosphere strongly influences our climate and weather as it contributes to the Earth's radiative budget and transports energy in the form of latent heat. Knowing exactly

how water vapor is distributed in the vertical improves our understanding of basic processes like cloud formation, moist convection and mixing. However, the quantification of these processes still comes with large uncertainties which limits the accuracy of climate prediction models [1]. A more detailed picture of the role of atmospheric moisture in the water cycle, and thus additional constraints for numerical models, can be obtained by incorporating an analysis of its isotopic composition. Due to fractionation processes during phase changes, stable water isotopologues serve as natural tracers helping to identify the origin of water vapor and providing insights into its condensation and evaporation history [2]. Of nine possible water isotopologues, this paper focuses on the detection of the most abundant  $\text{H}_2^{16}\text{O}$  (99.73098%, hereafter referred to as  $\text{H}_2\text{O}$ ) and the semi-heavy water isotopologue  $\text{HD}^{16}\text{O}$  (0.031460%, hereafter referred to as HDO). Isotopic abundances are often expressed using the so-called  $\delta$ -notation, which compares the ratio of the heavy (HDO) to the light isotopologue ( $\text{H}_2\text{O}$ ) with the standard abundance ratio of Vienna Standard Mean Ocean Water (VSMOW) [3]:

$$\delta D = \left[ \frac{[\text{HDO}]_{\text{sample}}/[\text{H}_2\text{O}]_{\text{sample}}}{[\text{HDO}]_{\text{VSMOW}}/[\text{H}_2\text{O}]_{\text{VSMOW}}} - 1 \right] \cdot 1000, \quad (1)$$

with  $[\text{HDO}]_{\text{VSMOW}}/[\text{H}_2\text{O}]_{\text{VSMOW}} = 3.1152 \times 10^4$ .

Isotopic water vapor in the atmosphere is measured either by in situ instruments or by passive remote sensing from the ground or from space. Today, most in situ instruments are based on laser spectrometry, e.g. cavity-ring-down spectrometers (CRDS), providing real-time measurements of multiple water isotopologues with high precision and accuracy. For instance, reported precisions in  $\delta D$  for commercial CRDS analyzers are in the range of 5–10‰ [4], but also precision levels close to 1‰ have been reported [5]. In situ observations can be conducted on the ground [5,6] or by using specially equipped aircraft [7–9]. Remote sensing instruments operated on the ground are usually Fourier transform infrared (FTIR) spectrometers which provide total column measurements of  $\text{H}_2\text{O}$  and HDO. They can be organized in networks, such as the Total Carbon Column Observing Network (TCCON) [10], providing  $\delta D$  columns with a precision between 5‰ and 35‰ (see Table 4 of Risi et al. [11] and references therein). From space,  $\text{H}_2\text{O}$  and HDO are observed using spectrometers operating in the thermal infrared spectral range such as the Infrared Atmospheric Sounding Interferometer (IASI) onboard the MetOP satellite [12,13]. They are mostly sensitive in the stratosphere and free troposphere, but instruments operating in the short-wave infrared (SWIR), such as the Japanese Greenhouse Gases Observing Satellite (GOSAT) [14] and the more recent Tropospheric Monitoring Instrument (TROPOMI) onboard the Sentinel-5 Precursor (S5P) satellite [15], also have good sensitivity in the lower troposphere which contains the majority of atmospheric water vapor.

$\text{H}_2\text{O}$ /HDO data products from satellite-borne observations have significantly contributed to improve our understanding of the tropical water cycle [16] and to assess the role of plants in global evapotranspiration [17]. However, due to their lack of vertical resolution, oftentimes reduced sensitivity in the boundary layer and insufficient temporal coverage, they are ill-suited for the study of the dynamics of evaporation, condensation, and air mass mixing processes on local or regional scales. For such type of observation, vertically resolved  $\text{H}_2\text{O}$ /HDO profiles have to be obtained by in-situ sensors mounted on airborne platforms in the frame of dedicated measurement campaigns. For example, Sodemann et al. [7] investigated the isotopic composition of water vapor in the marine boundary layer over the western Mediterranean using a CRDS analyzer onboard an aircraft. More recently, Chazette et al. [9] deployed a CRDS, among other sensors, onboard an ultra-light aircraft to gain insights into the vertical distribution of stable water isotopologues above an Alpine mountain lake in order to analyze their links with the isotopic composition of the lake water and with location-characteristic small-scale dynamics.

Laser active remote sensing is another promising technology to provide such data with high spatio-temporal resolution. For  $\text{H}_2\text{O}$ , Raman LIDARs have evolved as a robust and reliable tool

to probe its vertical distribution in the troposphere and they are nowadays routinely used in the framework of measurement campaigns [9,18,19]. For HDO however, no more than theoretical considerations are reported in the literature indicating that the realization of such an instrument is hindered by the low Raman cross-section [20]. Differential absorption LIDAR (DIAL) is another laser remote sensing method which exploits the difference in atmospheric transmission of short laser pulses at different, closely spaced wavelengths, provided that the absorption cross-section spectrum of the target molecule is well known [21]. Water vapor DIAL systems have been developed relying on pulsed laser sources emitting in the visible and near infrared [22–24]. Development efforts have also been dedicated to multiple-wavelength DIAL instrumentation in the spectral range between 1.5  $\mu\text{m}$  to 2.05  $\mu\text{m}$  as it allows the co-located monitoring of multiple greenhouse gases [24]. This approach can help reduce the bias induced by water vapor on the retrieval of dry-air mixing ratios of carbon dioxide ( $\text{CO}_2$ ), which is especially relevant in the prospect of integrated-path DIAL monitoring of  $\text{CO}_2$  from space [25].

The multi-species DIAL approach has a potential for water isotopic ratio detection which is equivalent to a two-species measurement provided that both isotopologues have similarly suitable and well-separated absorption lines. Indeed, Yu et al. [26] recently demonstrated range-resolved LIDAR measurements of HDO together with  $\text{CO}_2$ . But no LIDAR system existed up until now to provide range-resolved measurements of HDO together with the main isotopologue  $\text{H}_2\text{O}$  which would enable the estimation of  $\delta\text{D}$  with high spatio-temporal resolution as shown in our sensitivity study [27].

Here, we present first results of vertical, range-resolved measurements of the stable water isotopologues  $\text{H}_2\text{O}$  and HDO in the boundary layer using a ground-based differential absorption LIDAR, named WaVIL (for Water Vapor and Isotope Lidar), based on a parametric laser source at 1.98  $\mu\text{m}$  which was integrated in a mobile LIDAR truck with the prospect of future field campaigns. The rest of this paper is organized as follows. Section 2. describes the theoretical background of the DIAL method and briefly presents the spectroscopy and line selection in the 1.98  $\mu\text{m}$  operating range. Section 3. is dedicated to the LIDAR instrument setup. The laser architecture is presented and the wavelength meter calibration procedure is described. In Sec. 4, measurement conditions are detailed and a description of auxiliary measurements for comparison is given. Then, results are presented for two separate retrievals of  $\text{H}_2\text{O}$  and HDO profiles. Random and systematic errors are discussed in the form of an error budget including an estimation of the error in the isotopic abundance  $\delta\text{D}$ . A final conclusion is given in Sec. 5.

## 2. Two-wavelength DIAL method

### 2.1. DIAL retrieval method

The DIAL technique consists in measuring the backscattered light intensity of a laser beam sent into the atmosphere which wavelength is alternately tuned to (on-line) and away from (off-line) an absorption line of the atmospheric gas of interest. The variation in atmospheric transmission between the on-line and off-line signals is then used to determine the gas concentration over some range. Starting from the LIDAR equation [28], the backscattered power signal arriving at the detection unit as a function of range  $r$  can be expressed as:

$$P_r(r) = T_r \frac{A}{r^2} \beta_\pi(r) O(r) \frac{c}{2} T_{\text{atm}}^2(r) E_p, \quad (2)$$

where  $T_r$  is the receiver transmission,  $A$  is the effective area of the receiving telescope,  $\beta_\pi(r)$  is the atmospheric backscatter coefficient,  $O(r)$  is a function accounting for the geometric overlap between laser beam and telescope field of view,  $c$  is the speed of light,  $E_p$  is the laser pulse energy and  $T_{\text{atm}}(r)$  is the one-way atmospheric transmission. The atmospheric transmission depends on the extinction coefficients accounting for molecular absorption ( $\alpha_{\text{abs}}$ ) and for Mie and Rayleigh

scattering ( $\alpha_{\text{scat}}$ ) according to:

$$T_{\text{atm}}(\lambda, r) = \exp\left(-\int_0^r (\alpha_{\text{abs}}(\lambda, r') + \alpha_{\text{scat}}(\lambda, r')) dr'\right). \quad (3)$$

For the case of a pulsed two-wavelength DIAL, it is assumed that the on-line and off-line laser pulses are emitted sufficiently close in wavelength and time to consider backscatter coefficient  $\beta_{\pi}$  and scattering extinction coefficient  $\alpha_{\text{scat}}$  as constant. The resulting transmission for both pulses thus depends only on the wavelength-dependent absorption along the line of sight and the difference in transmission is expressed in terms of the single-path differential absorption optical depth according to:

$$\Delta\tau(r) = \frac{1}{2} \ln\left(\frac{P_{\text{off}}(r)}{P_{\text{on}}(r)}\right), \quad (4)$$

with  $P_{\text{off}}(r)$  and  $P_{\text{on}}(r)$  as the received power signals for the off-line and on-line wavelengths, respectively. From the absorption optical depth measurement, the mixing ratio of H<sub>2</sub>O or HDO can be calculated as columnar average  $X_{\text{col}}$  between two points  $r_1$  and  $r_2$  (integrated-path measurement) according to:

$$X_{\text{col}} = \frac{\Delta\tau(r_2) - \Delta\tau(r_1)}{\int_{r_1}^{r_2} WF(r) dr}, \quad (5)$$

where  $WF(r)$  is a weight function defined as:

$$WF(r) = [\sigma_{\text{on}}(r) - \sigma_{\text{off}}(r)] \rho_{\text{air}}(r), \quad (6)$$

with  $\sigma_{\text{on}}(r)$  and  $\sigma_{\text{off}}(r)$  as the on- and off-line absorption cross-sections of the target molecule and  $\rho_{\text{air}}(r)$  as the total air number density. For the case of vertical soundings, Eq. (6) is range-dependent since air number density and absorption cross-sections depend on the vertical profiles of pressure and temperature. This requires an a priori knowledge of these two quantities either by using an atmospheric model based on measurements at ground level or by relying on auxiliary observations along the LIDAR line of sight (radiosondes, Raman-LIDAR). The implication of uncertainties in the atmospheric parameters on the DIAL retrieval is discussed in the error budget.

Range-resolved concentration measurements are obtained by repeatedly applying a local integrated-path measurement according to Eq. (5) at a remote range  $r$  within a range bin  $\Delta r$ . The local volume mixing ratio can then be written as:

$$X(r) = \frac{1}{WF(r)} \frac{d}{dr} \Delta\tau(r). \quad (7)$$

## 2.2. Spectroscopy and line selection

In a previous theoretical study we identified the spectral window between 1982 nm and 1985 nm as suitable for H<sub>2</sub>O and HDO DIAL measurements in the lower troposphere. Indeed, this spectral range contains well separated absorption lines of H<sub>2</sub>O and HDO with no interference of other atmospheric trace gases [27]. Figure 1(a) shows the spectrum of the H<sub>2</sub>O and HDO optical depths calculated for a 1 km path under standard atmospheric conditions (15°C and 1013.25 hPa) and relative humidity of 50% using the line parameters of the HITRAN2020 database [29]. The H<sub>2</sub>O on-line wavelength is located at 5043.0475 cm<sup>-1</sup> (1982.93 nm) and the off-line wavelength at 1982.25 nm. The HDO isotopologue is sounded at 5040.4937 cm<sup>-1</sup> (1983.93 nm) with an off-line wavelength close to 1983.80 nm. As shown in Fig. 1(a), the differential absorption is significantly higher for H<sub>2</sub>O (0.45 over 1 km with constant mixing ratio of 5 g kg<sup>-1</sup>) compared to the differential absorption of HDO (0.06 over 1 km assuming  $\delta D = 0$ ). This has implications on

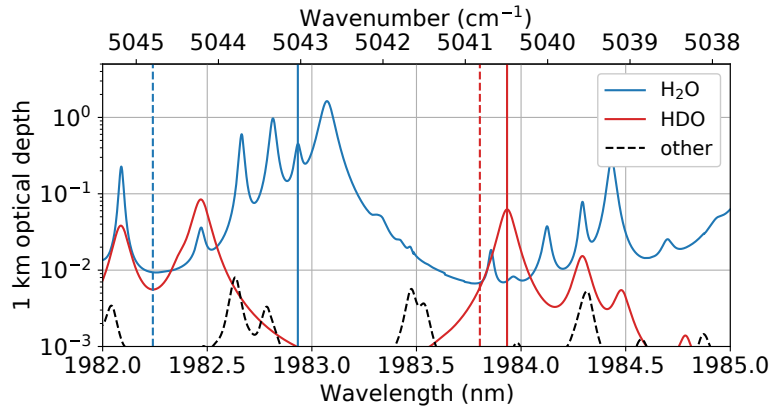


**Fig. 1.** Spectrum of the optical depth over a 1 km path with uniform mixing ratios of H<sub>2</sub>O and HDO corresponding to a relative humidity of 50% at 15°C and standard atmospheric pressure ( $\delta D = 0$  assumed for HDO). Dashed black line: other trace gases (CO<sub>2</sub>, CH<sub>4</sub>, N<sub>2</sub>O) assuming typical atmospheric concentrations. Solid and dashed vertical lines: positions of on-line and off-line wavelengths.

the range bin size used for the DIAL retrieval as the random error is inversely proportional to the differential absorption cross-section (see Eqs. (5) and (6)).

For the calculation of the absorption cross-sections, we use a Voigt line shape model of the form:

$$\sigma(\nu) = \sigma_0 \frac{y}{\pi} \int_{-\infty}^{+\infty} \frac{\exp(-t^2)}{y^2 + (x-t)^2} dt, \quad (8)$$

with

$$\begin{aligned} \sigma_0 &= \frac{S}{\gamma_D} \left( \frac{\ln 2}{\pi} \right)^{1/2}, \\ y &= \frac{\gamma}{\gamma_D} (\ln 2)^{1/2}, \\ x &= \frac{\nu - \nu_0}{\gamma_D} (\ln 2)^{1/2}, \end{aligned}$$

where  $S$  is the line strength,  $\gamma_D$  is the Doppler half width at half maximum (HWHM),  $\gamma$  is the pressure-broadened linewidth (HWHM) and  $\nu_0$  is the line center position. The line strength depends on the temperature  $T$  and the energy of the lower molecular state  $E''$  according to [21]:

$$S = S_0 \left( \frac{T_0}{T} \right)^{3/2} \exp \left[ \frac{E'' hc}{k} \left( \frac{1}{T_0} - \frac{1}{T} \right) \right], \quad (9)$$

where  $T_0$  is the reference temperature,  $k$  is the Boltzmann constant and  $c$  is the speed of light. Table 1 provides an overview of key spectroscopic parameters from the HITRAN2020 database for the H<sub>2</sub>O and HDO absorption lines of interest. Note the difference in the lower-state energy  $E''$  between H<sub>2</sub>O and HDO. A higher value for H<sub>2</sub>O gives rise to a higher temperature sensitivity. This implies some a priori knowledge of the temperature profile along the LIDAR line of sight in order to limit retrieval biases (see error budget in Sec. 4.4).

**Table 1. Spectroscopic parameters for selected DIAL absorption lines from the HITRAN2020 database.  $\nu$ : vacuum wavenumber,  $\lambda$ : vacuum wavelength,  $S$ : line intensity at 296 K,  $\gamma_{\text{air}}$ : air-broadened half width at half maximum (HWHM) at 296 K and reference pressure of 1 atm (1013.25 hPa),  $E''$ : lower-state energy**

	$\nu$ cm <sup>-1</sup>	$\lambda$ nm	$S$ cm <sup>-1</sup> (molec·cm <sup>-2</sup> ) <sup>-1</sup>	$\gamma_{\text{air}}$ cm <sup>-1</sup> atm <sup>-1</sup>	$E''$ cm <sup>-1</sup>
H <sub>2</sub> O	5043.0476	1982.928	$2.17 \times 10^{-24}$	0.0367	920.21
HDO	5040.4937	1983.933	$9.38 \times 10^{-25}$	0.1003	116.46

**Table 2. WaVIL system specifications**

<b>Transmitter</b>		
On/off-line wavelengths H <sub>2</sub> O	1982.933 nm / 1982.287 nm	
On/off-line wavelengths HDO	1983.933 nm / 1983.803 nm	
Pulse repetition frequency	150 Hz	150 Hz on/off switch rate
Pulse energy	5–7 mJ	
Pulse length	12 ns (FWHM)	
Linewidth	< 100 MHz (FWHM)	
Full beam divergence	0.3 mrad	
Wavelength monitoring	Wavelength meter (pulse to pulse)	High Finesse WS-6-200-IR2
<b>Receiver</b>		
Telescope diameter / focal length	25.4 cm / 75 cm	Newton-type
Field of view	1.2 mrad	defined by 900 $\mu$ m fiber
Detector type	PIN InGaAs photodiode	Hamamatsu G12182-003K
Detector diameter	300 $\mu$ m	
Transimpedance amplifier gain	10 <sup>6</sup> V/A	FEMTO DHPA-100
Bandwidth	3.5 MHz	
Noise-equivalent power (NEP)	1.3 pW Hz <sup>-1/2</sup>	
Digitizer	8 bits, 500 MHz sampling	Agilent U1084A

### 3. WaVIL instrument setup

#### 3.1. LIDAR architecture

##### 3.1.1. Transmitter

The DIAL transmitter is based on a master-oscillator-power-amplifier (MOPA) architecture consisting of an optical parametric oscillator (OPO) and an optical parametric amplification (OPA) stage. A schematic setup of the DIAL transmitter and receiver is shown in Fig. 2 and a summary of key system parameters is provided in Table 2. The master oscillator is a doubly-resonant nested-cavity OPO (NesCOPO) which is a versatile frequency synthesizer based on parametric down-conversion of a near-IR primary radiation for which laser technology is well matured to wavelengths in the 2–10  $\mu$ m range offering the potential for various gas sensing applications [30]. For the here presented DIAL system, the NesCOPO features a Periodically Poled Lithium Niobate (PPLN) crystal (type 2 quasi phase matching) converting the 1.06  $\mu$ m pump radiation from a Nd:YAG laser to a 1.98  $\mu$ m signal and 2.30  $\mu$ m idler radiation. Owing to the Vernier spectral filtering provided by the doubly resonant architecture, the NesCOPO-emitted radiation is single-frequency without the need for any injection-seeding laser [31]. It is coarsely tunable over several nanometers via the PPLN crystal temperature and fine-tunable within the NesCOPO parametric gain bandwidth of 1 nm by adjusting the cavity lengths using piezoelectric

transducers. Wavelength control via the cavity lengths is used for pulse-to-pulse switching between the DIAL on- and off-line wavelengths. Changing between the H<sub>2</sub>O and HDO DIAL spectral ranges requires wavelength tuning over more than 1 nm (see Fig. 1) and is realized by slightly changing the NesCOPO operating temperature. The signal wavelength is monitored (pulse-to-pulse) with a commercial wavelength meter (High Finesse WS6 IR). The OPA stage consists of three high-aperture (5x7 mm<sup>2</sup>) periodically poled Potassium Titanyl Phosphate (PPKTP) crystals [32] and is pumped by the Nd:YAG laser with 12 ns pulses carrying 70 mJ of energy per pulse. Based on this configuration and by filtering the idler beam prior to the last crystal for enhanced conversion efficiency, signal output energies for DIAL operation range from 5–7 mJ. The amplified signal beam is then filtered and passes a beam expander resulting in a divergence full-angle of approximately 300  $\mu$ rad.

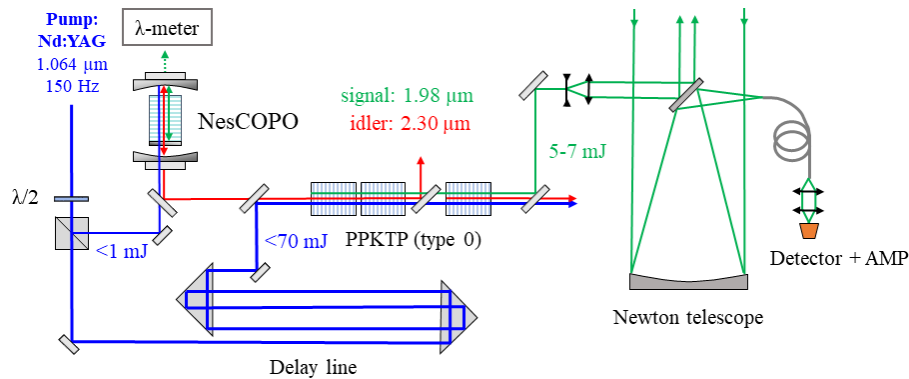


**Fig. 2.** Schematic WaVIL instrument architecture. NesCOPO: nested-cavity optical parametric oscillator, PPKTP: periodically poled Potassium Titanyl Phosphate crystals, AMP: amplifier.

### 3.1.2. Receiver and data acquisition

The LIDAR receiver consists of a 10-inch-aperture Newton telescope and a 900  $\mu$ m-diameter multimode fiber in the focal plane resulting in a full field-of-view angle of 1.2 mrad. The fiber output mode is imaged onto an InGaAs PIN photodiode (Hamamatsu G12182-003K) with an aperture of 300  $\mu$ m operated under room-temperature. The photodiode-generated current is amplified by a transimpedance amplifier with a gain setting of  $10^6 \text{ V A}^{-1}$  resulting in a bandwidth of 3.5 MHz and a noise-equivalent power (NEP) of  $1.3 \text{ pW Hz}^{-1/2}$ . The amplified signals are digitized using an 8-bit high speed digitizer (Agilent U1084A) featuring a 500 MHz sampling rate and a bandwidth of 20 MHz.

### 3.2. Wavelength meter calibration and stability

Because the mixing ratio retrieval depends on the absorption cross-sections at the on- and off-line wavelengths, an accurate knowledge of the laser-emitted wavelengths is crucial to limit biases. Therefore, care has to be taken to calibrate the wavelength meter and to estimate the uncertainty related to the wavelength reading during DIAL operation.

Measurements by wavelength meters can be subject to drifts induced by temperature and pressure changes in the instrument environment which cannot always be accounted for in the wavelength calculation [33]. To gain an insight into the magnitude of this type of wavelength deviation, we used our wavelength meter to record the wavelength of a laser diode emitting at 1560 nm locked to a hyperfine transition of rubidium-87 atoms (<sup>87</sup>Rb). Figure 3(a) shows the observed wavelength drift over a duration of 90 min. The recording was performed under

temperature-stabilized laboratory conditions and shows wavelength fluctuations of 30 MHz (peak to peak) which is in line with the accuracy of 40 MHz stated in the wavelength meter data sheet. However, wavelength monitoring under less temperature-stable conditions such as field campaigns is expected to induce larger drifts. It is thus important to calibrate the wavelength meter regularly.

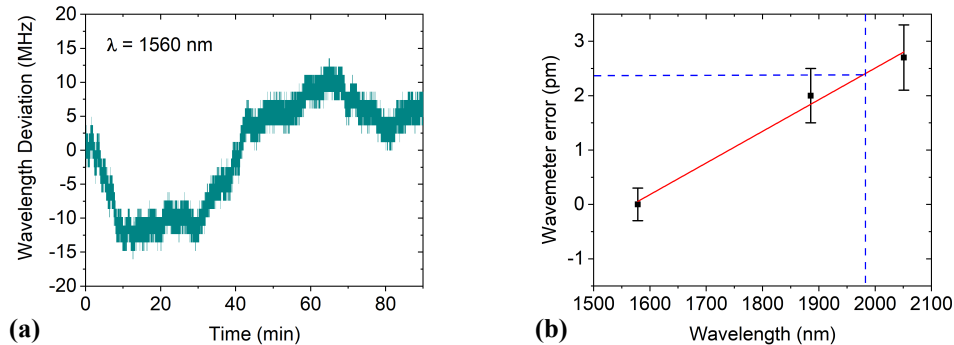


**Fig. 3.** (a) High Finesse WS6 IR wavelength meter stability over 90 min determined by monitoring the wavelength of a 1560 nm laser diode locked to a hyperfine transition of  $^{87}\text{Rb}$  atoms. (b) Difference between wavelength meter reading and actual wavelength of a laser diode locked to a  $\text{CO}_2$  or  $\text{H}_2\text{O}$  absorption line after calibration at 1579 nm. Error bars indicate uncertainty due to the laser diode locking stability. Vertical and horizontal dashed lines indicate the DIAL wavelength range at  $1.98\ \mu\text{m}$  and the corresponding wavelength error of 2.4 pm, respectively.

With no calibration source at hand at the DIAL wavelength around 1983 nm and the calibration software requiring wavelengths below 2000 nm, we first used a laser diode locked to a  $\text{CO}_2$  absorption line at 1579 nm to calibrate the wavelength meter. Since this wavelength is over 400 nm below the water vapor DIAL wavelengths, an additional laser diode locked to a  $\text{CO}_2$  absorption line at 2051 nm (closest to the DIAL wavelength of 1983 nm) is used to quantify the difference between the theoretical wavelength of the absorption peak and the wavelength meter reading, which is in the order of  $2.7 \pm 0.6\ \text{pm}$  at 2051 nm (see Fig. 3(b)). Assuming a linear increase for the observed differences in wavelength meter measurement and transition-locked diode wavelength, we estimate a wavelength correction term of  $-2.4\ \text{pm}$  that has to be applied to all wavelength meter readings at the DIAL wavelengths around 1983 nm. As a final estimate of the wavelength uncertainty for the error budget a value of 1 pm (75 MHz) is used. This accounts for possible wavelength drifts during the DIAL measurement and the uncertainty related to the procedure of determining the described wavelength correction applied to all DIAL wavelengths around 1983 nm.

## 4. DIAL measurements of $\text{H}_2\text{O}$ and $\text{HDO}$

### 4.1. Measurement conditions and auxiliary instruments

DIAL measurements of the two stable water vapor isotopologues were performed on 23 March 2022 at the facilities of ONERA (Office national d'études et de recherches aérospatiales,  $48.71^\circ\text{N}$ ,  $2.23^\circ\text{E}$ ) located on the Saclay plateau approximately 15 km south of Paris (see Fig. 4). With a water vapor mixing ratio of  $3.5\ \text{g kg}^{-1}$  measured on the ground, the atmosphere was relatively dry. Figure 5 shows the aerosol backscatter signal over the entire day of 23 March 2022 obtained by a cloud and aerosol ceilometer (1064 nm) operated by the SIRTa observatory (Site Instrumental de Recherche par Télédétection Atmosphérique [34],  $48.71^\circ\text{N}$ ,  $2.21^\circ\text{E}$ ) also located on the Saclay plateau only 2 km to the west of ONERA. It indicates cloud-free conditions with aerosols trapped

in the boundary layer stretching up to a height of 2 km. Apart from a sensor for meteorological parameters such as temperature, pressure and humidity next to the LIDAR at ground level, we compare the DIAL-retrieved H<sub>2</sub>O profile with a measurement obtained by balloon-borne radio sounding launched at 12:00 UTC at the Météo-France site of Trappes (48.77° N, 2.01° E) which is located about 17 km to the west of ONERA.

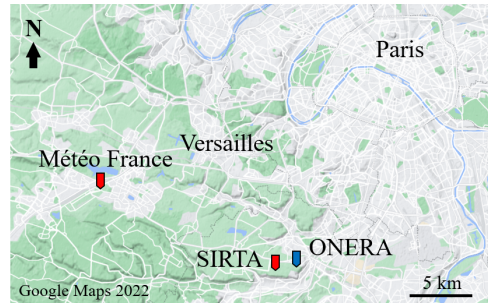


**Fig. 4.** Overview map of the different observation locations at the Saclay plateau in the south-western Paris region. The DIAL instrument was located the ONERA site. Aerosol backscatter profiles were measured at the SIRTA observatory. A vertical humidity profile was measured at the Météo France station of Trappes. Map credit: © Google Maps 2022

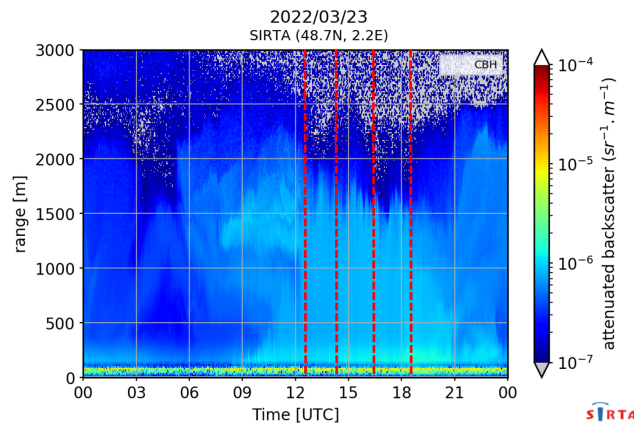


**Fig. 5.** Ceilometer measurement of the attenuated backscatter coefficient at the SIRTA observatory on 23 March 2022. Vertical dashed lines indicate time windows during which DIAL measurements of H<sub>2</sub>O and HDO were performed at ONERA. Figure credit: © SIRTA 2022

#### 4.2. Retrieved vertical profiles of H<sub>2</sub>O and HDO

Two separate measurements of H<sub>2</sub>O and HDO were conducted consecutively between 12:25 and 13:20 UTC on 23 March 2022. A 5 min-long interruption separates both measurements due to routine checks and the need to adjust the NesCOPO operating temperature in order to switch from the H<sub>2</sub>O to the HDO spectral range. Figure 6(a) shows the received on- and off-line LIDAR signals of the H<sub>2</sub>O measurement expressed as signal-to-noise ratios (SNR) resulting from time averaging over 25 min (ca. 60 000 valid on/off laser shot pairs). With the dominant noise contribution related to the transimpedance amplifier (1.3 pW Hz<sup>-1/2</sup> noise-equivalent power), the reported SNRs take account for detection noise only. The SNR is calculated by dividing the

received signal voltage by the standard deviation of a pre-trigger signal. The lower off-line SNR in Fig. 6(a) is the consequence of a less energetic cavity mode emitted by the NesCOPO at the off-line wavelength. Figure 6(b) presents the H<sub>2</sub>O raw-data differential optical depth (DOD) derived from the on- and off-line signals according to Eq. (4) which is utilized for the mixing ratio retrieval. The DOD standard error is calculated from the SNR of the on- and off-line signals according to:

$$\sigma_{\text{DOD}}(r) = \frac{1}{2} \sqrt{\frac{1}{\text{SNR}_{\text{ON}}^2(r)} + \frac{1}{\text{SNR}_{\text{OFF}}^2(r)}}. \quad (10)$$

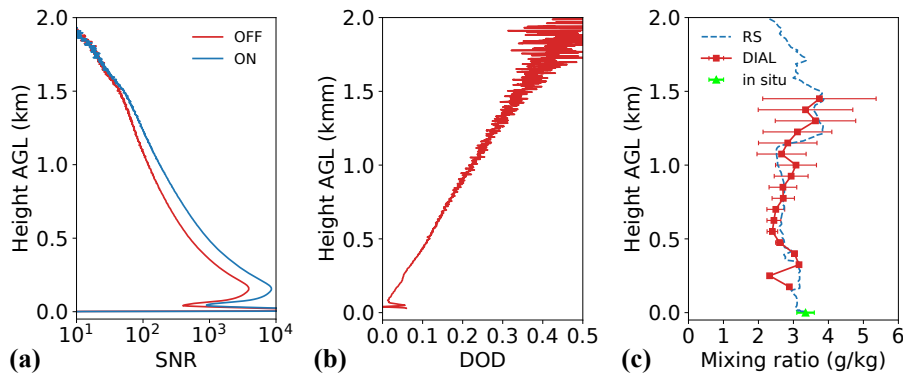


**Fig. 6.** DIAL measurement results for H<sub>2</sub>O from 12:25 to 12:50 UTC (ca. 60 000 valid on/off shot pairs). (a) Raw (no energy normalization) signal-to-noise ratios of the on- and off-line LIDAR returns. (b) Recorded differential optical depth. (c) DIAL-retrieved profile of the H<sub>2</sub>O mixing ratio (150 m range cells and 75 m sampling) compared to radiosonde (RS) profile and ground-based in situ sensor (accuracy ca. 0.25 g/kg).

According to Eq. (7), the volume mixing ratio at a given range has to be calculated from the local slope of the DOD. To evaluate the derivative in Eq. (7) a linear least-square estimator within each range bin is used and the local mixing ratio is then given by the slope of the linear regression and its random error is determined by the standard error of the regression.

The retrieved vertical profile of the H<sub>2</sub>O mixing ratio is plotted in Fig. 6(c). The depicted profile was retrieved from the measured DOD using range cells of 150 m and a sampling of 75 m. As a first means of validation of the obtained profile, the DIAL measurement is compared with a radiosonde in situ measurement launched 17 km away from the WaVIL operation site. The DIAL-retrieved profile compares fairly well to the radiosounding and also to the water vapor content measured by a humidity sensor directly at the LIDAR on the ground.

In a second validation experiment, the LIDAR was operated continuously over two hours from 16:30 UTC to 18:30 UTC on the same day to measure the time evolution of the vertical profile of H<sub>2</sub>O with a time resolution of 8 min. Figure 7 shows the resulting time series for the first point of the DIAL-retrieved profiles at 175 m above ground level (a.g.l.) compared to the in situ point sensor located on the ground. The observed difference between both measurements can most likely be explained by the fact that the water vapor concentration is slightly higher in the surface layer where the in situ probe is located as it is also the case in the H<sub>2</sub>O profile measured earlier on that day shown in Fig. 6(c). Despite the difference in the measured mixing ratios at ground level and at 175 m a.g.l., a clear correlation is apparent between the in situ and the DIAL measurements proving well the H<sub>2</sub>O sensitivity of the WaVIL instrument to small variations in the atmospheric water vapor concentration.

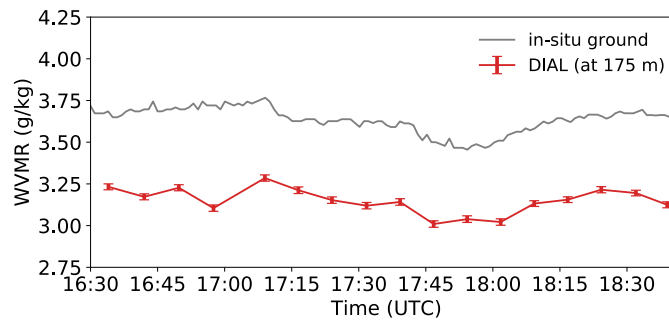


**Fig. 7.** Two-hour continuous H<sub>2</sub>O DIAL measurement from 16:30 UTC to 18:30 UTC (8 min time resolution) and comparison between water vapor mixing ratio measured in situ on the ground and the first DIAL measurement point at 175 m above ground level. The accuracy of the point sensor is 0.25 g/kg.

The averaged return signals (ca. 70 000 valid on/off shot pairs) and the DOD of the HDO measurement are depicted in panels (a) and (b) of Fig. 8. Due to the significantly lower differential absorption of HDO, and thus more noise in the obtained DOD, the range bin size of the retrieval has to be significantly increased in order to limit the resulting random error at the cost of range resolution. In the derived HDO profile shown in Fig. 8(c), range cells of 600 m and a spatial sampling of 300 m are used. With no reference measurement of HDO available during the operation of the WaVIL instrument, the retrieved HDO profile is compared to an estimated range of the HDO mixing ratio calculated from the H<sub>2</sub>O radiosonde profile (spatially averaged using 300 m range bins) and assuming uniform values for  $\delta D$  between  $-50\text{‰}$  and  $-200\text{‰}$ , which are typical values to be found in the lower troposphere [7–9,35]. Both thus-obtained profiles are plotted in Fig. 8(c) alongside the DIAL-retrieved profile showing good agreement to within the retrieval standard errors. The error bars in the retrieved profiles result from the standard error of the regression used to evaluate the slope of the differential optical depth. Altitude-dependent absorption cross-sections are calculated based on vertical profiles of temperature (lapse rate of  $-6.5 \text{ K km}^{-1}$ ) and pressure calibrated to ground sensor measurements next to the LIDAR.

#### 4.3. Estimation of the isotopic abundance $\delta D$

Using the DIAL-measured HDO profile and a profile of H<sub>2</sub>O retrieved earlier with the same vertical resolution (600 m range bins and 300 m sampling), the HDO isotopic abundance  $\delta D$  was derived from the two measurements according to Eq. (1). The resulting values of  $\delta D$  range from  $-51\text{‰}$  at 0.4 km a.g.l. to  $-119\text{‰}$  at 1.3 km a.g.l. with random errors of  $20\text{‰}$  and  $337\text{‰}$ , respectively. It is worth noting that  $\delta D$  is not determined from simultaneous measurements of H<sub>2</sub>O and HDO but from two consecutive and independent measurements. Due to the fact that for each sounding LIDAR signals are accumulated over a duration of 25 min, any change in the atmospheric water vapor content between both measurements results in a biased  $\delta D$  calculation. For instance, the H<sub>2</sub>O mixing ratio measured by the point sensor at ground level decreased slightly by ca. 1.5% within 30 min between the H<sub>2</sub>O and the HDO DIAL measurement. Assuming that the water vapor content within the first few hundreds of meters is correlated to changes at ground level (see Fig. 7), the 1.5% change in the H<sub>2</sub>O mixing ratio would lead to a  $15\text{‰}$  bias in  $\delta D$ .

The isotopic abundance  $\delta D$  is an indicator of phase change conditions in the atmosphere that occur during the transport of air parcels at various scales, evidencing processes such as mixing, evaporation and condensation since the fractionation degree depends on the meteorological conditions, e.g. temperature and level of saturation [7]. For instance, low  $\delta D$  values (typically  $-150\text{‰}$ ) in atmospheric water vapor at the surface indicate low air mass temperatures and

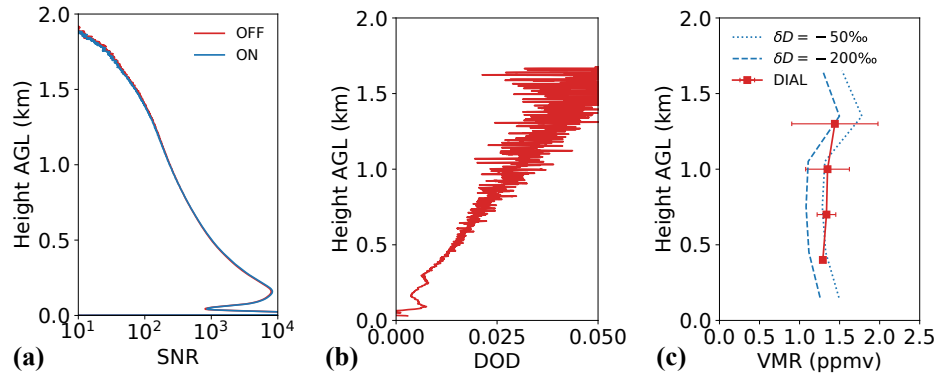


**Fig. 8.** DIAL measurement results for HDO from 12:55 to 13:20 UTC (ca. 70 000 valid on/off-shot pairs). (a) Raw (no energy normalization) signal-to-noise ratios of the on- and off-line LIDAR returns. (b) Recorded differential optical depth. (c) DIAL-retrieved profile of the HDO volume mixing ratio (600 m range cells and 300 m sampling). Dotted and dashed lines are drawn to guide the eye, indicating calculated HDO profiles based on the H<sub>2</sub>O radiosonde profile (spatially averaged using 300 m range bins) and uniform  $\delta D$  values of  $-50\text{‰}$  and  $-200\text{‰}$ .

strong rainout of air parcels [36,37], whereas high  $\delta D$  (typically  $-80\text{‰}$ ) values indicate high air mass temperatures and recent mixture of fresh ocean evaporate. Using an airborne CRDS analyzer above an alpine mountain lake, Chazette et al. [9] reported  $\delta D$  observations ranging between  $-80\text{‰}$  near the surface and  $-335\text{‰}$  around 3.5 km above mean sea level. Over the Mediterranean, Sodemann et al. [7] reported airborne  $\delta D$  observations between  $-97\text{‰}$  near the sea surface and  $-225\text{‰}$  in the free troposphere around 3.5 km above sea level. At mid-latitudes, increasing depletion with height is also generally observed based on airborne in situ observations [7,9,38].

#### 4.4. Error budget analysis

Table 3 gives a summary of different error sources contributing to the total error budget in the H<sub>2</sub>O and HDO DIAL measurements, and finally  $\delta D$ , over a 1.5 km range under the meteorological and instrumental conditions of the DIAL tests on 23 March 2022. Random errors are principally due to noise in the detection unit. For an integration time of 25 min, the precision in the water vapor mixing ratio was estimated as  $0.1 \text{ g kg}^{-1}$  (2.5% relative error) at 0.4 km above the ground and  $0.6 \text{ g kg}^{-1}$  (20%) at 1 km for 150 m range bins. For HDO and with 600 m range bins, the relative error at the first DIAL point at 0.4 km a.g.l. is 2% and grows to 37% at 1.3 km. Using this range bin size for the retrieval of H<sub>2</sub>O yields a 0.5% relative error at 0.4 km and 8.4% at 1.3 km. With respect to  $\delta D$  this amounts to absolute random errors of 20‰ and 337‰ at 0.4 km and 1.3 km a.g.l., respectively.

Systematic errors arise from uncertainties in the knowledge of spectroscopic, atmospheric and instrument parameters used to compute the weight function  $WF$  (see Eq. (6)) for the mixing ratio retrieval. The sensitivity of  $WF$  to the uncertainty in a parameter  $Y$  was estimated by generating a random set of numbers  $\delta Y$  that follow a normal distribution with a mean of zero and a standard deviation  $\sigma_Y$  (assumed uncertainty in  $Y$ ). This random seeding was used to calculate  $WF(Y + \delta Y)$  for each  $\delta Y$  and the relative error  $\epsilon$  in  $WF$ , and thus in the retrieved mixing ratio, is evaluated from the mean of the perturbed weight function  $\overline{WF}(Y + \delta Y)$  according to

$$\epsilon = \frac{|WF(Y) - \overline{WF}(Y + \delta Y)|}{WF(Y)}. \quad (11)$$

**Table 3. Budget of random and systematic errors for DIAL measurements of H<sub>2</sub>O and HDO up to a height of 1.5 km with the WaVIL instrument. Random errors for 600 m range bins for H<sub>2</sub>O and HDO. Assumed uncertainties of spectroscopic parameters from HITRAN2020 database if stated therein. (\*) marks uncertainties with no estimates in HITRAN2020 for which case an assumed value is used. Systematic errors were calculated using a random-seeding approach (see text for details).**

Error source	H <sub>2</sub> O		HDO		δD
	Uncertainty	Rel. error	Uncertainty	Rel. error	Abs. error
<b>Detection (random error)</b>					
at 400 m		0.5%		2.0%	20‰
at 700 m		2.5%		8.7%	92‰
at 1000 m		4.6%		20.2%	192‰
at 1300 m		8.4%		37.4%	337‰
<b>Transmitter</b>					
Wavelength accuracy	±1 pm (75 MHz)	0.5%	±1 pm (75 MHz)	0.1%	5‰
<b>Spectroscopy</b>					
Line position	±0.001 cm <sup>-1</sup>	0.2%	±0.0001 cm <sup>-1</sup>	negligible	2‰
Line intensity	±2%	1.6%	±2%	1.6%	22‰
Air-broadened width $\gamma_{\text{air}}$	±2%	0.5%	±10%	9.3%	89‰
T-exponent of $\gamma_{\text{air}}$	±10%*	0.1%	±10%*	0.4%	4‰
Pressure shift	±20%*	0.4%	±20%*	negligible	4‰
<b>Atmosphere</b>					
Temperature	±3 K	1.9%	±3 K	0.9%	20‰
Pressure	±5h Pa	0.2%	±5h Pa	0.1%	2‰
Total systematic error		2.6%		9.5%	94‰

The first category of systematic errors is related to uncertainties in the spectroscopic line parameters from the HITRAN2020 database. If stated therein, line parameter uncertainties are used for the error estimation. With respect to line position, the stated uncertainty of 0.001 cm<sup>-1</sup> translates into a relative error of 0.2% in the retrieved H<sub>2</sub>O mixing ratio. For HDO, the stated uncertainty is even smaller so that the resulting systematic error is negligible. For both H<sub>2</sub>O and HDO, a 2% uncertainty is assumed for the line intensity parameter giving rise to relative errors of 1.6% for both isotopologues resulting in a 22‰ absolute error in δD. Uncertainties for the air-broadened width stated in HITRAN2020 differ with 2% for H<sub>2</sub>O and 10% for HDO. While this leads to an error of 0.5% in the retrieved H<sub>2</sub>O mixing ratio, the HDO retrieval is very sensitive to the high uncertainty leading to an error of 9.3% and an absolute error in δD of 89‰. This makes it the largest systematic δD error and the dominant error contribution in the lower boundary layer up to the point where the random error begins to dominate at around 0.7 km a.g.l. With respect to the temperature exponent of the air-broadened width, an uncertainty of 10% results in relative errors of 0.1% and 0.4% for H<sub>2</sub>O and HDO, respectively. This translates into an error in δD of 4‰. Uncertainties for the pressure shift parameters are not stated in HITRAN2020. A conservative assumption of 20% leads to 0.4% relative error for H<sub>2</sub>O and a negligible error for HDO.

The next category includes systematic errors due to uncertainties in the a priori profiles of atmospheric pressure and temperature used for the isotopologue retrieval. Because the presented DIAL measurements rely on temperature and pressure model profiles calibrated only to the point sensor measurement on the ground, we use relatively conservative uncertainties of 3 K and 5 hPa for temperature and pressure, respectively. For the more temperature-sensitive H<sub>2</sub>O isotopologue this leads to a relative error of 1.9% and a pressure error of 0.2%. HDO is less sensitive to

uncertainties in the temperature and pressure profiles with relative errors of 0.9% and 0.1%. This leads to errors in  $\delta D$  of 20‰ and 2‰ due to temperature and pressure, respectively.

The major instrument-related systematic error stems from the uncertainty of the wavelength meter reading at the on-line wavelength. As described in Sec. 3.2, this error is principally determined by the accuracy of the wavelength meter and the uncertainty related to the calibration process which is estimated to be 1 pm (75 MHz). The resulting relative errors are around 0.5% and 0.1% for H<sub>2</sub>O and HDO, respectively, which translates into an absolute error in  $\delta D$  of 5‰.

An additional wavelength-related systematic error can arise from the position of the on-line wavelength at the absorption peak and eventual fluctuations thereof. Figure 9 shows histograms of the measured on-line wavelengths for both the H<sub>2</sub>O and HDO measurement. For the H<sub>2</sub>O measurement, the on-line wavelengths have a standard deviation of 0.1 pm (11 MHz), which is close to the wavelength meter resolution. Similarly for HDO, the on-line wavelengths have a standard deviation of 0.2 pm (16 MHz). Variations in the emitted on-line wavelengths of this order induce only very small variations in absorption (0.1% for H<sub>2</sub>O and 0.02% for HDO) which are negligible compared to the aforementioned uncertainty due to the accuracy of the wavelength meter and calibration procedure.

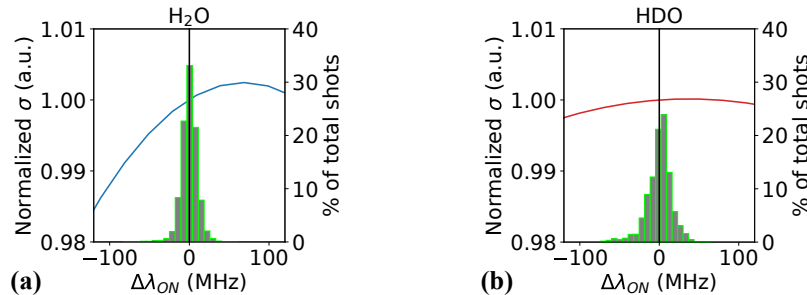


**Fig. 9.** Absorption cross-section  $\sigma$  (left y-axis) and histogram of on-line wavelengths (right y-axis) expressed as differences  $\Delta\lambda_{ON}$  from mean on-line wavelengths for H<sub>2</sub>O (a) and HDO (b). Absorption cross-sections are normalized to their values at the mean on-line wavelengths.

The total systematic error for the H<sub>2</sub>O mixing ratio is under 3% ( $<0.12 \text{ g kg}^{-1}$ ) and can be further reduced by limiting the uncertainty in the a priori temperature profile by the means of auxiliary measurements if available. A possible total systematic error of nearly 10% was estimated for HDO which is largely due to the uncertainty in the air-broadened width parameter stated in the HITRAN2020 database and which is the most significant contribution to the total error in the isotopic abundance  $\delta D$  in the first few hundreds of meters until the random error begins to dominate at around 0.7 km. This clearly demonstrates the need for dedicated spectroscopic studies in the spectral range of 1.98  $\mu\text{m}$  in order to reduce the line-parameter uncertainties.

## 5. Conclusions

In the context of observing stable water vapor isotopologues in the lower troposphere, the differential absorption LIDAR WaVIL capable of probing the water vapor isotopologues H<sub>2</sub>O and HDO in the atmospheric boundary layer was presented. The WaVIL transmitter is based on a parametric laser source generating nanosecond pulses with energies around 5 mJ at 1.98  $\mu\text{m}$  where both isotopologues have distinct absorption lines. First vertical measurements were conducted at a suburban site close to Paris with a maximum range of 1.5 km which is principally determined by the aerosol structure as the DIAL signals rely solely on aerosol backscattering in this wavelength range. For an integration time of 25 min, the precision (random error) in the water vapor mixing

ratio was estimated as  $0.1 \text{ g kg}^{-1}$  (2.5% relative error) at 0.4 km above the ground and  $0.6 \text{ g kg}^{-1}$  (20%) at 1 km for 150 m range bins. The DIAL-measured  $\text{H}_2\text{O}$  profile agrees well with an in situ radiosonde measurement and a good correlation to a point sensor measurement next to the LIDAR on the ground was demonstrated over a two-hour long duration. Measuring HDO is more challenging because its absorption is significantly weaker. Relative precision similar to  $\text{H}_2\text{O}$  for the same averaging time can only be achieved at the cost of spatial resolution (600 m range bins).

From the consecutive DIAL measurements of  $\text{H}_2\text{O}$  and HDO the isotopic abundance  $\delta\text{D}$  was estimated, although with an uncertainty in the range of or larger than typical tropospheric  $\delta\text{D}$  values under midlatitude conditions ( $-50\text{‰}$  to  $-200\text{‰}$ ). Measured values of  $\delta\text{D}$  are  $-51\text{‰}$  at 0.4 km above the ground and  $-119\text{‰}$  in the upper part of the boundary layer at 1.3 km with random errors of  $20\text{‰}$  and  $337\text{‰}$ , respectively.

An error budget was presented taking account for uncertainties related to spectroscopic and atmospheric parameters as well as the accuracy of the wavelength meter. For  $\text{H}_2\text{O}$ , a total systematic error of 2.6% was estimated with the principal contributions stemming from uncertainty in the HITRAN2020 line intensity parameter and the a priori temperature profile used in the mixing ratio retrieval. The estimated systematic error for HDO is close to 10% which is mainly due to the uncertainty in the air-broadened width parameter stated in HITRAN2020 resulting in a total systematic  $\delta\text{D}$  error of  $94\text{‰}$ . This is larger than the random error of  $20\text{‰}$  at 0.4 km a.g.l. However, the random error in  $\delta\text{D}$  grows fast and in the upper part of the boundary layer it is the major contribution to the error budget reaching values over  $300\text{‰}$  at 1.3 km.

Dedicated spectroscopic studies are highly needed in order to reduce the line-parameter-associated uncertainties. An additional bias in  $\delta\text{D}$  can be caused by changes in the water vapor content between the independent  $\text{H}_2\text{O}$  and HDO measurements which lasted ca. 25 min for each isotopologue due to the need for time averaging in order to achieve sufficient signal-to-noise ratios. This can be addressed by implementing a multiple-wavelength DIAL technique to measure both isotopologues simultaneously. This would be possible by using spectral lines within a 1 nm-window and by implementing a more complex wavelength-switching scheme with at least three wavelengths switched on a pulse-to-pulse basis.

As a first-generation instrument, the presented DIAL system still needs improvements on both the transmitter side to achieve laser energies in the tens of millijoule and the receiver side with a significant reduction of the detector noise in order to enable high-precision, range-resolved  $\delta\text{D}$  measurements over the entire boundary layer. Scaling of the laser output energy is the subject of our current work by using high-aperture PPKTP crystals in a two-stage amplification architecture [39]. A perspective for higher detection sensitivity would be the implementation of a detector based on the latest avalanche-photodiode technology [27].

A potential deployment scenario of the current DIAL system is the study of the water cycle in urban areas. Advancing the knowledge on the water vapor budget in major cities is particularly important in the wintertime when the atmospheric boundary layer is shallow (generally no more than a few hundred meters) and capped by a temperature inversion layer limiting exchanges with the free troposphere. In these conditions, the demonstrated near-range precision would be sufficiently high to allow for a meaningful characterization of the evolution of  $\delta\text{D}$  and to help distinguish between natural and anthropogenic surface sources of water vapor.

**Funding.** Agence Nationale de la Recherche (ANR-16-CE01-0009); Horizon 2020 Framework Programme (821868).

**Acknowledgments.** The authors acknowledge the provision of meteorological sounding data by the French national meteorological service Météo-France. The authors thank the SIRTA observatory for providing the LIDAR data displayed in this study. The authors would like to thank Frédéric Blouzon (DT-INSU) and Georges Durry (GSMA) for their contributions in the early part of the WaVIL project.

**Disclosures.** The authors declare no conflict of interest.

**Data availability.** Data underlying the results presented in this paper are not publicly available at this time but may be obtained from the authors upon reasonable request.

## References

1. B. Stevens and S. Bony, "What are climate models missing?" *Science* **340**(6136), 1053–1054 (2013).
2. J. Galewsky, H. C. Steen-Larsen, R. D. Field, J. Worden, C. Risi, and M. Schneider, "Stable isotopes in atmospheric water vapor and applications to the hydrologic cycle," *Rev. Geophys.* **54**(4), 809–865 (2016).
3. H. Craig, "Standard for Reporting Concentrations of Deuterium and Oxygen-18 in Natural Waters," *Science* **133**(3467), 1833–1834 (1961).
4. L. R. Johnson, Z. D. Sharp, J. Galewsky, M. Strong, A. D. Van Pelt, F. Dong, and D. Noone, "Hydrogen isotope correction for laser instrument measurement bias at low water vapor concentration using conventional isotope analyses: application to measurements from Mauna Loa Observatory, Hawaii," *Rapid Commun. Mass Spectrom.* **25**(5), 608–616 (2011).
5. H. C. Steen-Larsen, S. J. Johnsen, V. Masson-Delmotte, B. Stenni, C. Risi, H. Sodemann, D. Balslev-Clausen, T. Blunier, D. Dahl-Jensen, M. D. Ellehøj, S. Falourd, A. Grindsted, V. Gkinis, J. Jouzel, T. Popp, S. Sheldon, S. B. Simonsen, J. Sjolte, J. P. Steffensen, P. Sperlich, A. E. Sveinbjörnsdóttir, B. M. Vinther, and J. W. C. White, "Continuous monitoring of summer surface water vapor isotopic composition above the Greenland Ice Sheet," *Atmos. Chem. Phys.* **13**(9), 4815–4828 (2013).
6. V. Bastrikov, H. C. Steen-Larsen, V. Masson-Delmotte, K. Gribanov, O. Cattani, J. Jouzel, and V. Zakharov, "Continuous measurements of atmospheric water vapour isotopes in western Siberia (Kourovka)," *Atmos. Meas. Tech.* **7**(6), 1763–1776 (2014).
7. H. Sodemann, F. Aemisegger, S. Pfahl, M. Bitter, U. Corsmeier, T. Feuerle, P. Graf, R. Hankers, G. Hsiao, H. Schulz, A. Wieser, and H. Wernli, "The stable isotopic composition of water vapour above Corsica during the HyMeX SOP1 campaign: insight into vertical mixing processes from lower-tropospheric survey flights," *Atmos. Chem. Phys.* **17**(9), 6125–6151 (2017).
8. C. Dyroff, S. Sanati, E. Christner, A. Zahn, M. Balzer, H. Bouquet, J. B. McManus, Y. González-Ramos, and M. Schneider, "Airborne in situ vertical profiling of HDO / H<sub>2</sub><sup>16</sup>O in the subtropical troposphere during the MUSICA remote sensing validation campaign," *Atmos. Meas. Tech.* **8**(5), 2037–2049 (2015).
9. P. Chazette, C. Flamant, H. Sodemann, J. Totems, A. Monod, E. Dieudonné, A. Baron, A. Seidl, H. C. Steen-Larsen, P. Doira, A. Durand, and S. Ravier, "Experimental investigation of the stable water isotope distribution in an Alpine lake environment (L-WAIVE)," *Atmos. Chem. Phys.* **21**(14), 10911–10937 (2021).
10. D. Wunch, G. C. Toon, J.-F. L. Blavier, R. A. Washenfelder, J. Notholt, B. J. Connor, D. W. T. Griffith, V. Sherlock, and P. O. Wennberg, "The Total Carbon Column Observing Network," *Philos. Trans. R. Soc., A* **369**(1943), 2087–2112 (2011).
11. C. Risi, D. Noone, J. Worden, C. Frankenberg, G. Stiller, M. Kiefer, B. Funke, K. Walker, P. Bernath, M. Schneider, D. Wunch, V. Sherlock, N. Deutscher, D. Griffith, P. O. Wennberg, K. Strong, D. Smale, E. Mahieu, S. Barthlott, F. Hase, O. Garcia, J. Notholt, T. Warneke, G. Toon, D. Sayres, S. Bony, J. Lee, D. Brown, R. Uemura, and C. Sturm, "Process-evaluation of tropospheric humidity simulated by general circulation models using water vapor isotopologues: 1. Comparison between models and observation," *J. Geophys. Res.: Atmos.* **117**(D5), D05303 (2012).
12. H. Herbin, D. Hurtmans, C. Clerbaux, L. Clarisse, and P.-F. Coheur, "H<sub>2</sub><sup>16</sup>O and HDO measurements with IASI/MetOp," *Atmos. Chem. Phys.* **9**(24), 9433–9447 (2009).
13. M. Schneider and F. Hase, "Optimal estimation of tropospheric H<sub>2</sub>O and δD with IASI/METOP," *Atmos. Chem. Phys.* **11**(21), 11207–11220 (2011).
14. C. Frankenberg, D. Wunch, G. Toon, C. Risi, R. Scheepmaker, J.-E. Lee, P. Wennberg, and J. Worden, "Water vapor isotopologue retrievals from high-resolution GOSAT shortwave infrared spectra," *Atmos. Meas. Tech.* **6**(2), 263–274 (2013).
15. A. Schneider, T. Borsdorff, J. aan de Brugh, A. Lorente, F. Aemisegger, D. Noone, D. Henze, R. Kivi, and J. Landgraf, "Retrieving H<sub>2</sub>O/HDO columns over cloudy and clear-sky scenes from the Tropospheric Monitoring Instrument (TROPOMI)," *Atmos. Meas. Tech.* **15**(7), 2251–2275 (2022).
16. J. Worden, D. Noone, and K. Bowman, "Importance of rain evaporation and continental convection in the tropical water cycle," *Nature* **445**(7127), 528–532 (2007).
17. S. P. Good, D. Noone, and G. Bowen, "Hydrologic connectivity constrains partitioning of global terrestrial water fluxes," *Science* **349**(6244), 175–177 (2015).
18. P. Chazette, C. Flamant, J.-C. Raut, J. Totems, and X. Shang, "Tropical moisture enriched storm tracks over the Mediterranean and their link with intense rainfall in the Cevennes-Vivarais area during HyMeX," *Q. J. R. Meteorol. Soc.* **142**, 320–334 (2016).
19. P. D. Girolamo, B. D. Rosa, C. Flamant, D. Summa, O. Bousquet, P. Chazette, J. Totems, and M. Cacciani, "Water vapor mixing ratio and temperature inter-comparison results in the framework of the Hydrological Cycle in the Mediterranean Experiment—Special Observation Period 1," *Bull. of Atmos. Sci. & Technol.* **1**(2), 113–153 (2020).
20. G. L. Liberti, D. Dionisi, F. Cheruy, and C. Risi, "Feasibility study to measure HDO/H<sub>2</sub>O atmospheric profiles through a Raman Lidar," *EPJ Web Conf.* **176**, 05032 (2018).
21. J. Bösenberg, "Differential-Absorption Lidar for Water Vapor and Temperature Profiling," in *Lidar – Range-Resolved Optical Remote Sensing of the Atmosphere*, (Springer-Verlag, 2005), pp. 213–239.
22. D. Bruneau, P. Quaglia, C. Flamant, M. Meissonnier, and J. Pelon, "Airborne lidar LEANDRE II for water-vapor profiling in the troposphere. I. System description," *Appl. Opt.* **40**(21), 3450–3461 (2001).

23. M. Wirth, A. Fix, P. Mahnke, H. Schwarzer, F. Schrandt, and G. Ehret, "The airborne multi-wavelength water vapor differential absorption lidar WALES: system design and performance," *Appl. Phys. B* **96**(1), 201–213 (2009).
24. G. A. Wagner and D. F. Plusquellic, "Multi-frequency differential absorption LIDAR system for remote sensing of CO<sub>2</sub> and H<sub>2</sub>O near 1.6 μm," *Opt. Express* **26**(15), 19420 (2018).
25. T. F. Refaat, U. N. Singh, J. Yu, M. Petros, S. Ismail, M. J. Kavaya, and K. J. Davis, "Evaluation of an airborne triple-pulsed 2 μm IPDA lidar for simultaneous and independent atmospheric water vapor and carbon dioxide measurements," *Appl. Opt.* **54**(6), 1387 (2015).
26. S. Yu, Z. Zhang, H. Xia, X. Dou, T. Wu, Y. Hu, M. Li, M. Shangguan, T. Wei, L. Zhao, L. Wang, P. Jiang, C. Zhang, L. You, L. Tao, and J. Qiu, "Photon-counting distributed free-space spectroscopy," *Light: Sci. Appl.* **10**(1), 212 (2021).
27. J. Hamperl, C. Capitaine, J.-B. Dherbecourt, M. Raybaut, P. Chazette, J. Totems, B. Grouiez, L. Régalia, R. Santagata, C. Evesque, J.-M. Melkonian, A. Godard, A. Seidl, H. Sodemann, and C. Flamant, "Differential absorption lidar for water vapor isotopologues in the 1.98 μm spectral region: sensitivity analysis with respect to regional atmospheric variability," *Atmos. Meas. Tech.* **14**(10), 6675–6693 (2021).
28. R. T. H. Collis and P. B. Russell, *Lidar measurement of particles and gases by elastic backscattering and differential absorption* (Springer Berlin Heidelberg, Berlin, Heidelberg, 1976), pp. 71–151.
29. I. Gordon, L. Rothman, R. Hargreaves, R. Hashemi, E. Karlovets, F. Skinner, E. Conway, C. Hill, R. Kochanov, Y. Tan, P. Weislo, A. Finenko, K. Nelson, P. Bernath, M. Birk, V. Boudon, A. Campargue, K. Chance, A. Coustenis, B. Drouin, J. Flaud, R. Gamache, J. Hodges, D. Jacquemart, E. Mlawer, A. Nikitin, V. Perevalov, M. Rotger, J. Tennyson, G. Toon, H. Tran, V. Tyuterev, E. Adkins, A. Baker, A. Barbe, E. Canè, A. Császár, A. Dudaryonok, O. Egorov, A. Fleisher, H. Fleurbaey, A. Foltynowicz, T. Furtenbacher, J. Harrison, J. Hartmann, V. Horneman, X. Huang, T. Karman, J. Karns, S. Kassi, I. Kleiner, V. Kofman, F. Kwabia-Tchana, N. Lavrentieva, T. Lee, D. Long, A. Lukashetskaya, O. Lyulin, V. Makhnev, W. Matt, S. Massie, M. Melosso, S. Mikhailenko, D. Mondelain, H. Müller, O. Naumenko, A. Perrin, O. Polyansky, E. Raddaoui, P. Raston, Z. Reed, M. Rey, C. Richard, R. Tóbiás, I. Sadiek, D. Schwenke, E. Starikova, K. Sung, F. Tamassia, S. Tashkun, J. Vander Auwera, I. Vasilenko, A. Viganin, G. Villanueva, B. Vispoel, G. Wagner, A. Yachmenev, and S. Yurchenko, "The HITRAN2020 molecular spectroscopic database," *J. Quant. Spectrosc. Radiat. Transfer* **277**, 107949 (2022).
30. J. B. Barria, D. Mammez, E. Cadiou, J. B. Dherbecourt, M. Raybaut, T. Schmid, A. Bresson, J. M. Melkonian, A. Godard, J. Pelon, and M. Lefebvre, "Multispecies high-energy emitter for CO<sub>2</sub>, CH<sub>4</sub>, and H<sub>2</sub>O monitoring in the 2 μm range," *Opt. Lett.* **39**(23), 6719 (2014).
31. A. Godard, M. Raybaut, and M. Lefebvre, "Nested Cavity Optical Parametric Oscillators (NesCOPO) - A tunable frequency synthesizer for Gas Sensing," in *Encyclopedia of analytical chemistry*, (John Wiley and Sons, Ltd, 2017).
32. A. Zukauskas, N. Thilmann, V. Pasiskevicius, F. Laurell, and C. Canalías, "5 mm thick periodically poled Rb-doped KTP for high energy optical parametric frequency conversion," *Opt. Mater. Express* **1**(2), 201–206 (2011).
33. K. König, P. Ingram, J. Krämer, B. Maaß, K. Mohr, T. Ratajczyk, F. Sommer, and W. Nörtershäuser, "On the performance of wavelength meters: Part 2—frequency-comb based characterization for more accurate absolute wavelength determinations," *Appl. Phys. B* **126**(5), 86 (2020).
34. M. Haefelin, L. Barthès, O. Bock, C. Boitel, S. Bony, D. Bouniol, H. Chepfer, M. Chiriaco, J. Cuesta, J. Delanoë, P. Drobinski, J.-L. Dufresne, C. Flamant, M. Grall, A. Hodzic, F. Hourdin, F. Lapouge, Y. Lemaître, A. Mathieu, Y. Morille, C. Naud, V. Noël, W. O'Hirok, J. Pelon, C. Pietras, A. Protat, B. Romand, G. Scialom, and R. Vautard, "SIRTA, a ground-based atmospheric observatory for cloud and aerosol research," *Ann. Geophys.* **23**(2), 253–275 (2005).
35. Z.-C. Zeng, O. Addington, T. Pongetti, R. L. Herman, K. Sung, S. Newman, A. Schneider, T. Borsdorff, Y. L. Yung, and S. P. Sander, "Remote sensing of atmospheric HDO/H<sub>2</sub>O in southern California from CLARS-FTS," *J. Quant. Spectrosc. Radiat. Transfer* **288**, 108254 (2022).
36. K. Yoshimura, M. Kanamitsu, and M. Dettlinger, "Regional downscaling for stable water isotopes: A case study of an atmospheric river event," *J. Geophys. Res.* **115**(D18), D18114 (2010).
37. H. Jacob and C. Sonntag, "An 8-year record of the seasonal variation of <sup>2</sup>H and <sup>18</sup>O in atmospheric water vapour and precipitation at Heidelberg, Germany," *Tellus B* **43**(3), 291–300 (1991).
38. M. Schneider, Y. González, C. Dyroff, E. Christner, A. Wiegele, S. Barthlott, O. E. García, E. Sepúlveda, F. Hase, J. Andrey, T. Blumenstock, C. Guirado, R. Ramos, and S. Rodríguez, "Empirical validation and proof of added value of MUSICA's tropospheric δD remote sensing products," *Atmos. Meas. Tech.* **8**(1), 483–503 (2015).
39. J. Hamperl, J. F. Geus, K. M. Mølster, A. Zukauskas, J.-B. Dherbecourt, V. Pasiskevicius, L. Nagy, O. Pitz, D. Fehrenbacher, H. Schaefer, D. Heinecke, M. Strotkamp, S. Rapp, P. Denk, N. Graf, M. Dalin, V. Lebat, R. Santagata, J.-M. Melkonian, A. Godard, M. Raybaut, and C. Flamant, "High Energy Parametric Laser Source and Frequency-Comb-Based Wavelength Reference for CO<sub>2</sub> and Water Vapor DIAL in the 2 μm Region: Design and Pre-Development Experimentations," *Atmosphere* **12**(3), 402 (2021).